PAPER

Exploring interfacial magnetism in all-spinel Fe₃O₄/MgCr₂O₄/Fe₃O₄ epitaxial heterostructures†

Francesco Offi, [a,b] Francesco Borgatti, [*c] Pasquale Orgiani, [b]
Vincent Polewczyk, [‡b] Sandeep Kumar Chaluvadi, [b] Shyni Punathum Chalil, [b]
Aleksandr Petrov,[b] Federico Motti, [b] Gian Marco Pierantozzi, [b]
Giancarlo Panaccione, [b] Bogdan Rutkowski, [d] Paolo Mengucci, [e,f]
Gianni Barucca, [e,f] Deepnarayan Biswas, [g] Tien-Lin Lee, [g]
Emiliano Marchetti,[a,j] Alberto Martinelli, [i] Davide Peddis [h,j] and
Gaspare Varvaro [j]

Epitaxial heterostructures integrating thin Fe₃O₄ films hold great potential for spintronics, magnetoionics, and multifunctional device development. In this work, the morpho-structural and magnetic properties of all-spinel Fe₃O₄/MgCr₂O₄/Fe₃O₄ trilayers grown on an MgCr₂O₄ buffer layer, exhibiting very close lattice matching, were investigated using both surface- and bulk-sensitive techniques. The close lattice match between Fe₃O₄ and MgCr₂O₄ enables the growth of epitaxial heterostructures with magnetically decoupled Fe₃O₄ layers for spacer thicknesses of ≥1.6 nm, while reducing the formation of antiphase boundaries. Despite localized interphase diffusion, which leads to the formation of a mixed Cr/Fe spinel oxide with magnetically polarized Cr ions at the Fe₃O₄/MgCr₂O₄ interfaces, the overall magnetic properties remain largely consistent with those of the individual Fe₃O₄ layers. This study sheds light on the magnetic interactions within Fe₃O₄ layers mediated by an MgCr₂O₄ spacer and demonstrates the feasibility of the approach in preserving the properties of thin Fe₃O₄ films in complex heterostructures, thus offering a promising pathway for designing advanced all-spinel oxide devices.

1. Introduction

Ferroic transition metal oxides (TMOs) have attracted a great deal of attention for both fundamental studies and technologi-

[a]Dipartimento di Scienze, Università Roma Tre, I-00146 Rome, Italy
[b]CNR – Istituto Officina dei Materiali (IOM), Area Science Park, I-34149 Trieste, Italy
[c]Istituto per lo Studio dei Materiali Nanostrutturati (ISMN), Consiglio Nazionale delle Ricerche (CNR), I-40129 Bologna, Italy. E-mail: francesco.borgatti@cnr.it
[d]AGH University of Krakow, Faculty of Metals Engineering and Industrial Computer Science, Kraków 30-059, Poland
[e]Department SIMAU, University Politecnica delle Marche, Via Brecce Bianche, I-60131 Ancona, Italy
[f]UdR INSTM, Ancona, Italy
[g]Diamond Light Source Ltd., Diamond House, Harwell Science and Innovation Campus, Didcot OX11 0DE, UK
[h]Università degli Studi di Genova, Dipartimento di Chimica e Chimica Industriale & INSTM RU, nM2-Lab, I-16146 Genova, Italy
[i]CNR-SPIN, I-16152 Genova, Italy
[j]National Research Council, Institute of Structure of Matter, nM2-Lab, Research Area Roma 1, Monterotondo Scalo, Roma, I-00015, Italy

†Electronic supplementary information (ESI) available. See DOI: https://doi.org/10.1039/d5nr00971e
‡Present address: Université Paris-Saclay, UVSQ, CNRS, GEMaC, 78000 Versailles, France.

cal applications.[1] The variable oxidation states of transition metals allow for the formation of several compounds, exhibiting a wide range of physical properties resulting from the strong coupling between charge, spin, orbital and lattice symmetry.[2,3] Novel functional materials, in the form of thin films, with tailored chemical and physical properties can be designed by changing the nature of each component or their relative thickness, or by tuning the interface interactions. Magnetic spinel oxides (MFe₂O₄) containing 3d metals (M = Fe, Co, Ni, Mn, etc.) represent one of the most interesting classes of TMOs due to their excellent chemical stability and rich crystal chemistry, allowing for excellent fine-tuning of the magnetic properties.[4,5]

Among family members, magnetite (Fe₃O₄) is of particular interest due to its unique magnetic and electrical properties.[6] Fe₃O₄ is a conductive and biocompatible material, showing ferrimagnetic characteristics, with a high Curie temperature (858 K), a theoretically predicted half-metal behavior and an experimentally observed spin polarization of almost 100% at the Fermi level.[7] These remarkable properties make Fe₃O₄ highly promising for various fields, including biomedicine,[8] spintronics,[9] magnetoionics,[10] soft robotics,[11] and multi-physics devices.[12] Owing to its peculiar properties, Fe₃O₄ films have been widely investigated as

key components of different thin film heterostructures, including hard/soft all-oxide composites, hybrid and all-oxide spintronic structures, and multilayers/superlattices consisting of magnetite thin films separated by a thin spacer layer.[13–24] Previous studies on Fe_3O_4-based multilayers/superlattices have demonstrated the richness of interface-induced phenomena occurring in such structures as a function of the spacer, including thickness-dependent anti-ferromagnetic/ferrimagnetic interface coupling, stabilization of thin magnetite layers, modulation of saturation magnetization and magnetic anisotropy.[17–23] The intricate interplay at the interface drives the magnetic characteristics of those structures, underscoring the significance of interface conditions in shaping the overall magnetic behaviour.[19,22,25] To date, only a few spacers, such as MgO, $MgFe_2O_4$, Mn_3O_4, $PtSe_2$, and TiN, have been explored, implying that there is potential to observe additional phenomena using alternative materials with selected characteristics.

In this work, we investigated the interface structure of Fe_3O_4-based trilayers consisting of thin ferrimagnetic Fe_3O_4 layers (7 nm) separated by an ultra-thin $MgCr_2O_4$ spacer with thicknesses of 0.6 nm, 1.6 nm and 2.4 nm grown on an $MgAl_2O_4$ (100) substrate covered with a thick $MgCr_2O_4$ buffer layer. $MgCr_2O_4$ is a spinel oxide exhibiting a favorable lattice parameter match with Fe_3O_4 ($a_{Fe_3O_4}$ = 8.394 Å, $a_{MgCr_2O_4}$ = 8.333 Å, where a_X is the lattice constant of the X compound).[26] Bulk $MgCr_2O_4$ is a semiconductive antiferromagnet that is paramagnetic above 12.5 K[27,28] and is expected to exhibit insulating behavior at low thicknesses, similar to other TMOs.[29] The same crystal symmetry and the comparable lattice constant are expected to result in epitaxial Fe_3O_4/$MgCr_2O_4$ heterostructures with coherently grown interfaces. Our results demonstrate that epitaxial structures indeed form, with the two Fe_3O_4 layers behaving independently for a spacer thickness of ≥1.6 nm. The heterostructure shows reduced coercivity compared to thick Fe_3O_4 films directly deposited on MgO (100) substrates, an effect attributed to a reduction of the antiphase boundary due to the excellent lattice match between Fe_3O_4 and the $MgCr_2O_4$ buffer layer. Although localized intermixing at the Fe_3O_4/$MgCr_2O_4$ interfaces induces magnetic polarization in Cr ions, this has minimal influence on the overall magnetic behaviour, which remains primarily governed by the individual Fe_3O_4 layers. These insights deepen our understanding of the magnetic interaction among spinel oxide layers, facilitating the development of functional full-oxide devices.

2. Experimental

Fe_3O_4/$MgCr_2O_4$/Fe_3O_4 thin film heterostructures were deposited on an $MgCr_2O_4$ buffer layer grown on single-crystal (100)-oriented $MgAl_2O_4$ spinel substrates by Pulsed Laser Deposition (PLD) at the NFFA laboratories, located within the Elettra synchrotron radiation facility in Trieste, Italy.[30] While ultraviolet excimer lasers (λ = 248 nm) are conventionally employed for the deposition of complex oxide heterostructures,[31] this study used a first harmonic Nd:YAG solid-state laser (1064 nm), which has recently demonstrated efficacy

in producing high-quality oxide films while offering a simpler experimental setup.[32–35] The deposition parameters were optimized for the individual Fe_3O_4 and $MgCr_2O_4$ layers, with the substrate temperature set to 500 °C. The growth was performed at laser repetition rates of 0.5 Hz and 1 Hz for Fe_3O_4 and $MgCr_2O_4$, respectively. Calibration of the growth rates via X-ray reflectivity yielded values of 0.02 nm and 0.008 nm per laser pulse, ensuring precise control over the layer thickness during deposition (see the ESI† for growth details). While a commercial target was used for Fe_3O_4, a home-made one was employed for $MgCr_2O_4$ (see the ESI† for fabrication details). To minimize the lattice mismatch between Fe_3O_4 and the substrate $[(a_{Fe_3O_4} - a_{MgAl_2O_4})/a_{MgAl_2O_4} \approx 3.8\%]$ and promote the formation of epitaxial thin films, the $MgAl_2O_4$ substrate was coated with a $MgCr_2O_4$ buffer layer with a nominal thickness of 30 nm, high enough to relax the strain induced by the substrate and reach the lattice parameter of bulk $MgCr_2O_4$, which closely matches that of the Fe_3O_4 layer, $[(a_{Fe_3O_4} - a_{MgCr_2O_4})/a_{MgCr_2O_4} \approx 0.7\%]$. The critical thickness t_c of $MgCr_2O_4$ on the $MgAl_2O_4$ substrate, above which the system exhibits strain relaxation, was estimated employing the Fischer, Kuhne, and Richards (FKR) model,[36] obtaining a value of about t_c = 17 nm (details are provided in the ESI†). On top of this buffer layer, trilayers consisting of two thin Fe_3O_4 films, each with a thickness of 7 nm, separated by an $MgCr_2O_4$ spacer with varying thicknesses (0.6 nm, 1.6 nm and 2.4 nm) were grown. For comparison, a thick Fe_3O_4 film with a thickness of 60 nm on the MgO (100) single-crystal substrate, and a single 7 nm thick Fe_3O_4 film deposited on $MgAl_2O_4$ (100), with and without an $MgCr_2O_4$ buffer layer, were grown under identical experimental conditions.

A comprehensive set of advanced measurements was conducted at room temperature to correlate the morpho-structural and magnetic properties of the samples. Magneto-optical Kerr effect (MOKE) measurements,[37] with a laser wavelength of 405 nm, as well as X-ray absorption spectroscopy (XAS) and X-ray magnetic circular dichroism (XMCD) investigation at the Cr and Fe $L_{2,3}$ absorption thresholds were executed under ultra-high vacuum conditions at the APE-HE beamline.[38] These latter measurements were performed in total electron yield (TEY) mode with the X-ray beam incident at 45° and an energy resolution of about 0.1 eV. The absorption spectra for XMCD were obtained in remanent magnetization after application of a ±0.05 T external magnetic field. In addition, HArd X-ray PhotoEmission Spectroscopy (HAXPES) measurements were conducted at the beamline I09 of the Diamond Light Source (UK),[39] on samples transported under a protective atmosphere and introduced into the experimental chamber without air exposure. Photon energies of $h\nu$ = 1.78, 4.05, and 8.08 keV (in all cases, the incidence angle was 20° from the sample surface) were set to obtain information at different depths, with total energy resolution at the different photon energies of 0.39, 0.25, and 0.27 meV, respectively. Structural characterization involved the use of ex situ X-ray reflectivity and a high-resolution scanning transmission electron microscope (HR-STEM). STEM observations on thin-film cross-sections (see the ESI† for details about sample preparation) were

performed using a probe Cs-corrected FEI Titan[3] G2 60-300 STEM equipped with ChemiSTEM technology (X-FEG field emission gun and Super-X EDX detector system) developed at FEI.[40] The latter allows for the chemical composition analysis of the layers down to the nanoscale with energy-dispersive X-ray (EDX) microanalysis. Integral magnetic measurements were performed at room temperature using a commercial MicroSense Model 10 vibrating sample magnetometer (VSM) with the magnetic field applied in the film plane along the (100) direction of the $MgAl_2O_4$ substrate. Semi-empirical calculations of the XAS and XMCD spectra were performed within the framework of the atomic multiplet and ligand field theory using the QUANTY program.[41] Details of the theoretical model can be found in the book by de Groot and Kotani.[42]

3. Results and discussion

3.1. Structural characterization

Fig. 1(a) and (b) present the crystallographic structures of Fe_3O_4 and $MgCr_2O_4$, highlighting the ion site occupancy, and the schematic structure of the multilayer, respectively. Fig. 1(c

and d) show high-resolution (HR) high-angle annular dark field (HAADF) STEM images of samples with $MgCr_2O_4$ spacer thicknesses of 0.6 and 2.4 nm, respectively. The high degree of epitaxial matching is evident in all the investigated samples, hence highlighting the structural quality of the whole hetero-structure (see also the noise-filtered images reported in Fig. SI1 and SI5 of the ESI†). The samples reveal the expected cubic structure (Fig. SI2 and SI6†) with the (001) planes parallel to the substrate surface, and pictures (c) and (d) are taken in the [100] and [110] zone-axis orientations.

Close inspection of the STEM image in panel (d) points out the presence of anti-phase boundaries (APBs) in the $MgCr_2O_4$ buffer layer, associated with displacement vectors of $a/4$ $\langle 110 \rangle$.[43,44] In the white square inset, the contrast variation in the periodic distribution of atoms in the $MgCr_2O_4$ buffer layer along the direction indicated by the dashed line is evident, and it is assigned to the presence of an $a/4$ $[1\bar{1}0]$ APB producing the corresponding shift of the $(\bar{1}11)$ lattice planes. Although generally expected in all samples, APBs are not visible in panel (c) because the sample is in the [100] zone-axis orientation and, as can be deduced from the inset of Fig. SI5(b),† a shift of $a/4$ $[011]$ of the lattice does not give rise
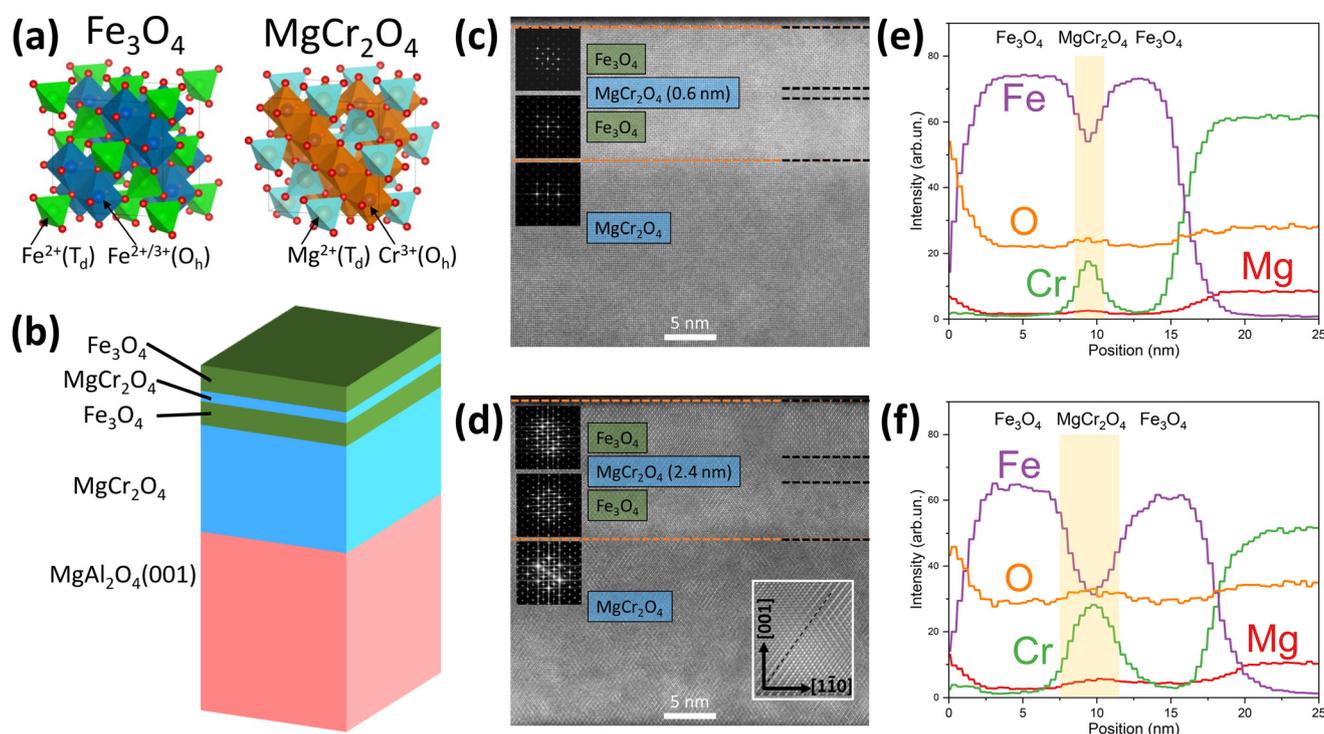

Fig. 1 (a) Inverse and normal spinel structures of Fe_3O_4 and $MgCr_2O_4$: in Fe_3O_4, a quarter of the tetrahedral positions of the lattice are occupied by Fe^{2+} ions, while half of the octahedral sites are occupied by Fe^{2+} and Fe^{3+} cations; in $MgCr_2O_4$, Mg^{2+} cations occupy the tetrahedral positions and Cr^{3+} cations occupy the octahedral ones. (b) Sketch of the $Fe_3O_4/MgCr_2O_4/Fe_3O_4$ heterostructure deposited on top of a thick $MgCr_2O_4$ buffer layer grown on the $MgAl_2O_4$ (001) substrate. (c and d) High-resolution HAADF-STEM images for heterostructures with $MgCr_2O_4$ spacers of 0.6 nm (c) and 2.4 nm (d). Black dashed lines indicate the different compound regions. The samples in panels (c) and (d) were [100] and [110] zone-axis oriented, respectively. Insets display FFTs performed in the corresponding regions of the heterostructures. The resulting interplanar distances are reported in Table 1. (e and f) Elemental distribution among the layers as achieved by STEM-EDX measurements. The intensity is not scaled to the formula unit composition. To better elucidate the details of STEM images, further information such as EDX elemental maps for Al, Mg, Fe, and Cr, and noise-filtered HR-STEM images are reported in Fig. SI1–SI7 of the ESI.†

to a new atomic distribution that can be distinguished by the Z (atomic number) contrast of the HAADF-STEM technique. The presence of APBs in the $MgCr_2O_4$ buffer layer is due to the formation of partial dislocations that relax the strain induced by the mismatch with the $MgAl_2O_4$ substrate.[36] The mismatch evolution across the whole heterostructure was investigated by performing fast Fourier transforms (FFTs) in different regions of the images [insets in Fig. 1(c) and (d)] and calculating the $d(040)$ and $d(220)$ interplanar distances, which are parallel to the substrate, reported in Table 1 [the values tabulated at the International Centre for Diffraction Data (ICDD) for $MgAl_2O_4$ (ICDD card no. 21-1152) were used to calibrate the FFT images]. The values listed in Table 1 show that the $MgCr_2O_4$ buffer layer is relaxed in proximity to the bottom Fe_3O_4 layer because its measured interplanar distances agree with the tabulated values for the bulk material (ICDD card no. 10-0351) within experimental errors. Similarly, the interplanar distances of the Fe_3O_4 layers are consistent with the bulk values (ICDD card no. 19-0629), indicating complete relaxation of the magnetite films. Despite the perfect lattice matching at the interface between the $MgCr_2O_4$ buffer layer and the Fe_3O_4 film, HR-STEM analysis reveals the presence of APBs in the Fe_3O_4/$MgCr_2O_4$/Fe_3O_4 trilayers (see Fig. SI3†). In this case, the origin of the APBs cannot be attributed to the mismatch between the cell parameters of the $MgCr_2O_4$ buffer layer and Fe_3O_4, since they show relaxed values, and therefore a comparable lattice parameter, but is more likely due to the propagation of the APB defects from the $MgCr_2O_4$ buffer layer to the Fe_3O_4/$MgCr_2O_4$/Fe_3O_4 trilayers. Noticeably, STEM-EDX measurements demonstrate that the elemental distribution inside the epitaxial heterostructures, shown in Fig. 1(c and d) and Fig. SI4–SI7,† is largely consistent with the actual thickness of each layer. These measurements are consistent with the results from the X-ray reflectivity analysis (see the ESI, Fig. S8†), which indicate the presence of relatively flat interfaces with a root mean square roughness of 0.2–0.3 nm. The elemental intensity profiles along the vertical direction are shown in panels (e and f) of Fig. 1, starting from the sample surface (left side) towards the $MgAl_2O_4$ substrate (right side). It is interesting to observe that Fe and Cr appear to diffuse into each other's layers at the top of the sample, and that the Fe signal is visible in the whole $MgCr_2O_4$ interlayer. Moreover, the spectral comparison clearly indicates that the Fe intensity significantly decreases as the distance from the interfaces increases for the 2.4 nm thick interlayer, thus suggesting a greater ability of the spacer to separate the magnetic phases as its thickness increases. Considering the presence of interdiffusion, the formation of regions with intermediate stoichiometries cannot be excluded.

3.2. Chemical states

The chemical states of Fe and Cr ions were investigated by core-level HAXPES. This information is particularly relevant to identify the presence of secondary phases formed during the growth, and/or at the boundaries between the layers that might also involve significant changes of the chemical states for the Fe and Cr ions. Fig. 2 shows the Fe 2p and Cr 2p core-level spectra of the thin film heterostructure with an $MgCr_2O_4$ spacer thickness of 0.6 nm. The spectra acquired for samples with thicker $MgCr_2O_4$ spacers provide similar results. With the incident photon energy varying from 1.78 keV to 8 keV, the information depth ranges from about 6 nm ($h\nu$ = 1.78 keV) to 25 nm ($h\nu$ = 8 keV), as sketched in the inset of panel (a); hence, the spectra refer to different regions of the heterostructure. Thus, the Fe 2p spectrum collected at 1.78 keV is related only to the upper Fe_3O_4 layer, consistent with the absence of Cr 2s and any spectral contribution of Cr in the survey spectrum (not shown here), suggesting that Cr diffusion in the top magnetite layer is mainly localized at the interface only. At higher photon energies, the Fe 2p spectra encompass the entire trilayer structure, and the Cr 2s and Cr 2p peaks [Fig. 2(b)] are also observed. Additionally, the Cr spectra for $h\nu$ = 4 keV are indicative only of the $MgCr_2O_4$ interlayer, while those for $h\nu$ = 8 keV contain a large bulk contribution from the underlying $MgCr_2O_4$ buffer layer. The latter thus provides a useful reference to distinguish changes in the electronic states of Cr ions in the thin $MgCr_2O_4$ interlayer.

The Fe 2p spectra shown in Fig. 2 exhibit typical characteristics of the Fe_3O_4 phase, as reported in previous studies.[45,46] The consistency of the spectra across a wide range of probing depths highlights the high quality of both magnetite layers and suggests the absence of significant deviations from the nominal stoichiometry. This conclusion is further supported by the fitting analysis of the Fe $2p_{3/2}$ peaks performed following the model described by Grosvenor et al., where the contribution of Fe^{2+} (Fe^{3+}) ions is identified at lower (higher) binding energies and each of the two is made up of several components deriving from multiplet splitting, surface components and satellites.[47] This analysis successfully disentangles the spectral term contributions from Fe^{2+} and Fe^{3+}, yielding an Fe^{3+}/Fe^{2+} intensity ratio of ~1.7, which is in good agreement with the expected ideal concentration ratio of 2:1. Note also that, in the spectral region between the two spin–orbit-split edges, the satellite structure that is prominent in the photoemission spectra of α-Fe_2O_3 (hematite) and γ-Fe_2O_3 (maghemite) is not visible in the present case.[48] Such a satellite structure is due to charge transfer screening and it is visible, at somewhat different binding energies, for iron oxides purely Fe^{2+} (such as FeO) or Fe^{3+} (such as Fe_2O_3), its intensity

Table 1 Interplanar distances obtained from FFTs of images taken from various regions of the heterostructure and for different $MgCr_2O_4$ interlayer thicknesses, as shown in Fig. 1(c) and (d). The top and bottom Fe_3O_4 layers were analyzed, yielding identical interplanar distances in both cases

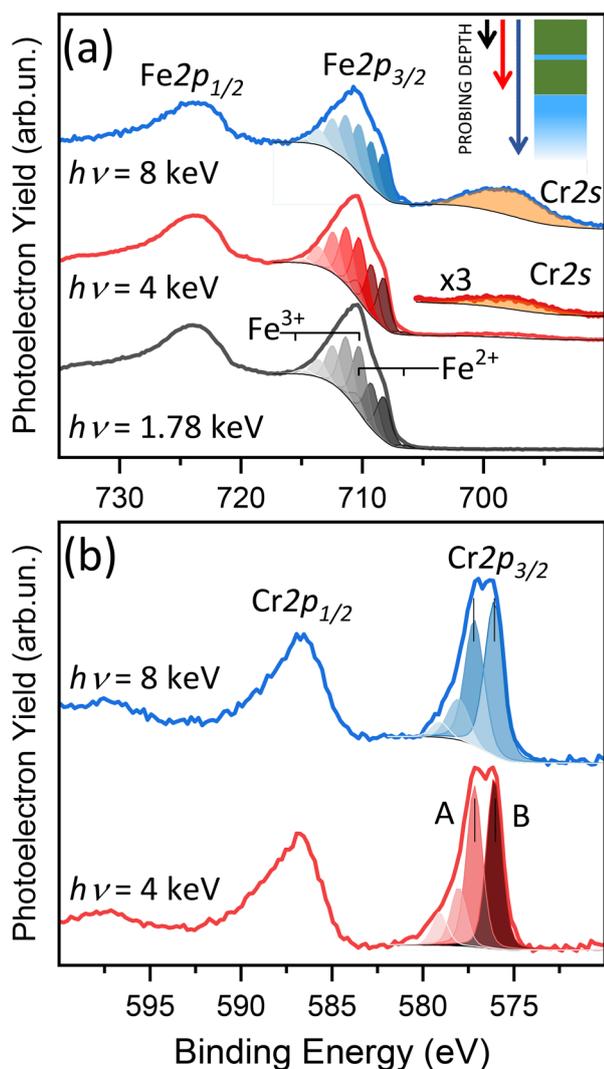|	Bulk material $d(040)$ (nm)	Bulk material $d(220)$ (nm)	$MgCr_2O_4$ 0.6 nm $d(040)$ (nm)	$MgCr_2O_4$ 2.4 nm $d(220)$ (nm)
Fe_3O_4	0.2099	0.2967	0.210 ± 0.002	0.296 ± 0.002
Fe_3O_4	0.2099	0.2967	0.210 ± 0.002	0.296 ± 0.002
$MgCr_2O_4$	0.2083	0.2945	0.206 ± 0.002	0.293 ± 0.002
$MgAl_2O_4$	0.2020	0.2858		

Fig. 2 Fe 2p (a) and Cr 2p (b) core-level spectra for the Fe₃O₄ (7 nm)/MgCr₂O₄ (0.6 nm)/Fe₃O₄ (7 nm) trilayer. Spectra are normalized to the maximum intensity. The Fe 2p spectra also show a Cr 2s peak located close to the Fe 2p$_{3/2}$ one. The information depth of the spectra, sketched in the inset of panel (a), ranges from about 6 nm ($h\nu$ = 1.78 keV) to 25 nm ($h\nu$ = 8 keV).

smearing out when both ionic components are present (such as in Fe₃O₄).[49] This implies that only magnetite is present in the investigated heterostructures and no other iron oxide phases are formed. This is particularly relevant for the Fe 2p spectrum for $h\nu$ = 1.78 keV, being the most sensitive to the surface.

The Cr 2s and Cr 2p spectra shown in panels (a) and (b), respectively, provide further confirmation of these results. The similarity of the spectra, despite the substantial differences in the probing depth, indicates that the chemical state of the Cr ions of the spacer closely resembles that of the thick MgCr₂O₄ buffer layer, suggesting the absence of secondary phases related to different chemical states, *e.g.* as Cr^{2+} in CrO₂. The multiplet splitting features resulting from the fitting analysis

of the Cr 2p$_{3/2}$ spectrum, with the energy splitting Δ_{AB} = 1.04–1.09 eV, resemble closely those of the α-Cr₂O₃ or CrFe₂O₄ phase, where the Cr^{3+} ions exclusively occupy octahedral lattice sites.[50,51] This strongly suggests that Cr ions in our sample predominantly reside in octahedral sites, as expected for the normal spinel structure of MgCr₂O₄. On the other hand, the observed spectral features are also compatible with the formation of a Cr/Fe mixed spinel oxide as long as this phase maintains the chemical state and site symmetry of the Fe and Cr ions. The formation of such a phase at both the Fe₃O₄/MgCr₂O₄ interfaces cannot be ruled out, and indeed it is the most plausible hypothesis to explain the observed magnetic measurements, as described in the following sections.

3.3. Magnetic investigation

The overall magnetic behaviour of the spinel oxide heterostructures is elucidated by a comparative study of VSM and MOKE measurements, as shown in Fig. 3 and Fig. SI9.† Field-dependent magnetization loops of thin film heterostructures for different MgCr₂O₄ spacer thicknesses are compared with that of a 7 nm thick Fe₃O₄ film deposited on the MgCr₂O₄ buffer layer to gain insights into the factors influencing the magnetic properties of the spinel oxide heterostructure. If we consider a penetration depth of the laser (λ = 400 nm) of about 20 nm,[52] the magnetic information obtained by MOKE measurements primarily relates to the thin film heterostructure and the MgCr₂O₄ buffer layer, while VSM provides the magnetization evolution of the entire sample, potentially including any magnetic contributions from the substrate. Due to the presence of ferro(i)magnetic impurities within the substrate, VSM measurements were corrected to account for both the diamagnetism of the substrate and the ferromagnetic contribution of the contaminants (Fig. SI10 in the ESI†). However, precise quantification of contamination levels in each sample proved challenging, impacting the correction's precision. This issue may lead to underestimations or overestimations of the magnetization value based on the correction method (as detailed in the ESI and shown in Fig. SI10†), especially in the high-field region, where the approach of magnetization to saturation can potentially be influenced by the presence of APBs.[53] Therefore, a reliable determination of the saturation magnetization is unfeasible. On the other hand, the correction had a minimal effect in the low-field region, as detailed in the ESI.† The agreement of the corrected VSM loops with the MOKE loops, collected in the ±0.1 T field region, supports the reliability of the magnetic measurements within this specific range, offering a dependable benchmark for studying and comparing samples' magnetic properties. Both the single Fe₃O₄ layer and the trilayers exhibit almost square loops, indicating a magnetically homogeneous film with a strong level of magnetic ordering.[54] Furthermore, the measured hysteresis loops reveal a relatively low coercive field, with $\mu_0 H_c$ = 7.0(5) mT for the single Fe₃O₄ layer, and $\mu_0 H_c$ = 12.5(5) mT, 6.5(3) mT and 5.0(3) mT for the trilayers containing MgCr₂O₄ spacers with thicknesses of 0.6 nm, 1.6 nm and 2.4 nm, respectively. These values are significantly lower than those observed for
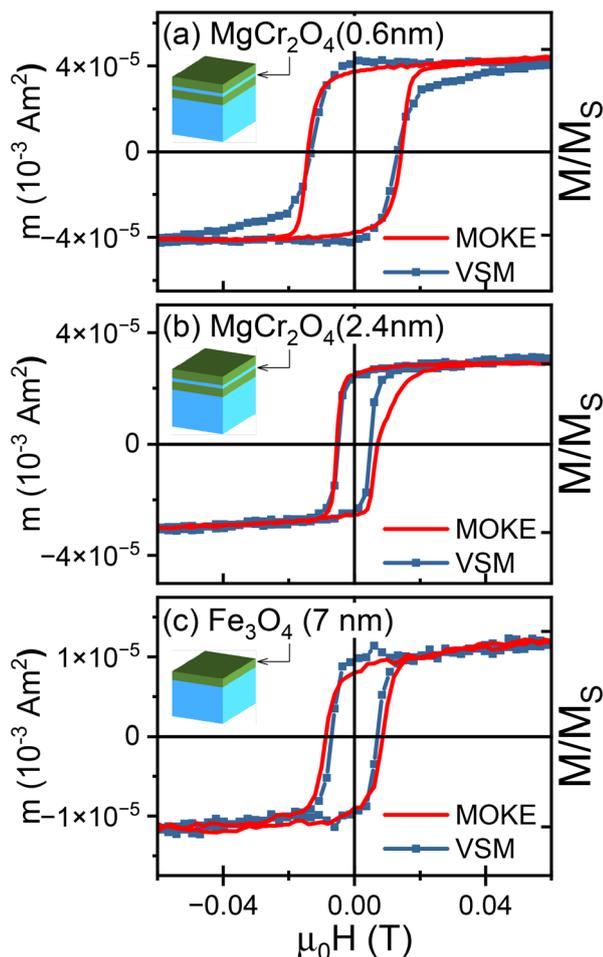
Fig. 3 (a and b) In-plane VSM (left scale) and longitudinal MOKE (right scale) field-dependent magnetization loops, $M(H)$, at 300 K of trilayer heterostructures with $MgCr_2O_4$ spacer thicknesses of (a) 0.6 nm and (b) 2.4 nm; (c) $M(H)$ loop of a 7 nm thick Fe_3O_4 reference film grown on an $MgCr_2O_4$ buffer layer.

Fe_3O_4 thin films deposited directly on $MgAl_2O_4$ (100) substrates without the $MgCr_2O_4$ buffer layer (see Fig. SI11 in the ESI†), thus suggesting that adding the $MgCr_2O_4$ buffer layer can reduce the density of APBs, typically resulting in increased coercivity through pinning effects.[55,56] Additionally, the similarity in coercivity between the trilayer with 1.6 nm and 2.4 nm thick $MgCr_2O_4$ spacers and the single Fe_3O_4 film suggests that the two magnetite films are effectively separated, behaving almost as individual entities. The rise in coercivity in the trilayer with a 0.6 nm thick $MgCr_2O_4$ spacer may be linked to the films' quasi-continuous nature, as greater thicknesses may correspond to higher coercivity, as observed in some studies focusing on similar low thickness regions.[53,57,58] This scenario could be somehow more complex if we consider the formation of a mixed Cr/Fe spinel oxide at the $Fe_3O_4/MgCr_2O_4$ interfaces, contributing to the overall magnetic configuration, as reported by Pinho *et al.* for the corresponding thin films.[59] Thus, besides the occurrence of APBs, the presence of mixed inter-

face phases could play a role in driving the magnetic properties of the entire heterostructure.

3.4. XAS and surface magnetic properties

Fig. 4 summarizes the XAS/XMCD results obtained for samples with $MgCr_2O_4$ spacer thickness ranging from 0.6 nm to 2.4 nm. The quantitative estimation of the XAS/XMCD depth sensitivity in total yield mode still remains incompletely defined. While it has been clarified that the sample depth probed by these measurements must be less than 20 nm,[60] XAS measurements of Fe $L_{2,3}$ absorption thresholds from Fe_3O_4 are reported with *mean probing depth* values from about 1 to 5 nm,[61,62] which demonstrates the high uncertainty in this value and the relatively high surface sensitivity of the technique. Therefore, we can safely assume that the spectra of Fig. 4 probe the upper part of the trilayer structure, *i.e.* the top Fe_3O_4 layer and the $MgCr_2O_4$ spacer, in particular excluding any contribution from the interface at the $MgCr_2O_4$ buffer layer. The X-ray absorption spectra of the Fe and Cr $L_{2,3}$ absorption thresholds for the sample with a $MgCr_2O_4$ spacer thickness of 0.6 nm, obtained by averaging over the dichroic curves, are shown in panels (a and b). Similar spectra (not shown) are obtained for the other $MgCr_2O_4$ spacer thicknesses. The Fe $L_{2,3}$ spectrum is consistent with most of those reported in the literature for magnetite, hence confirming the good quality of these layers.[63,64] On the other hand, the Cr $L_{2,3}$ spectrum is very similar to those of compounds hosting Cr^{3+} ($3d^3$) ions located in lattice sites with the local octahedral symmetry O_h, such as in Cr_2O_3,[59,65–67] thus reinforcing the hypothesis of having obtained the correct $MgCr_2O_4$ crystallographic structure, where indeed the chromium ions solely occupy the octahedral sites. Thus, the analysis of the Fe $L_{2,3}$ and Cr $L_{2,3}$ absorption spectra suggests that the heterostructure does not host spurious phases containing different oxidation states, which is in agreement with the HAXPES results. In particular, the absence of significant contributions by Cr^{2+} ions rules out the presence of room-temperature ferromagnetic CrO_2. In order to put these considerations on a firmer ground, we performed theoretical calculations, shown as red lines superimposed on the experimental spectra of Fig. 4(a) and (b), confirming the above interpretation: the Cr $L_{2,3}$ absorption spectrum was calculated for the Cr^{3+} valence state in octahedral local symmetry, consistently with the position of Cr ions in the $MgCr_2O_4$ lattice, while the calculation for the Fe $L_{2,3}$ absorption spectrum accurately incorporates the contribution of all Fe cations, *i.e.* Fe^{2+} in octahedral symmetry (O_h), Fe^{3+} in tetrahedral symmetry (T_d) and Fe^{3+} in octahedral symmetry (O_h). The calculations were performed for an infinite material and then adjusted to match the experimental intensity. In particular, for the iron case, the theoretical curve is obtained from the sum of the three different Fe contributions, weighted in order to obtain the best representation of the experimental data. The corresponding theoretical XMCD curves for each ion species are reported in panels (e and f).[63,64,68,69]

Although the shape and strength of the Fe XMCD are largely consistent with previous results on thin films of magne-
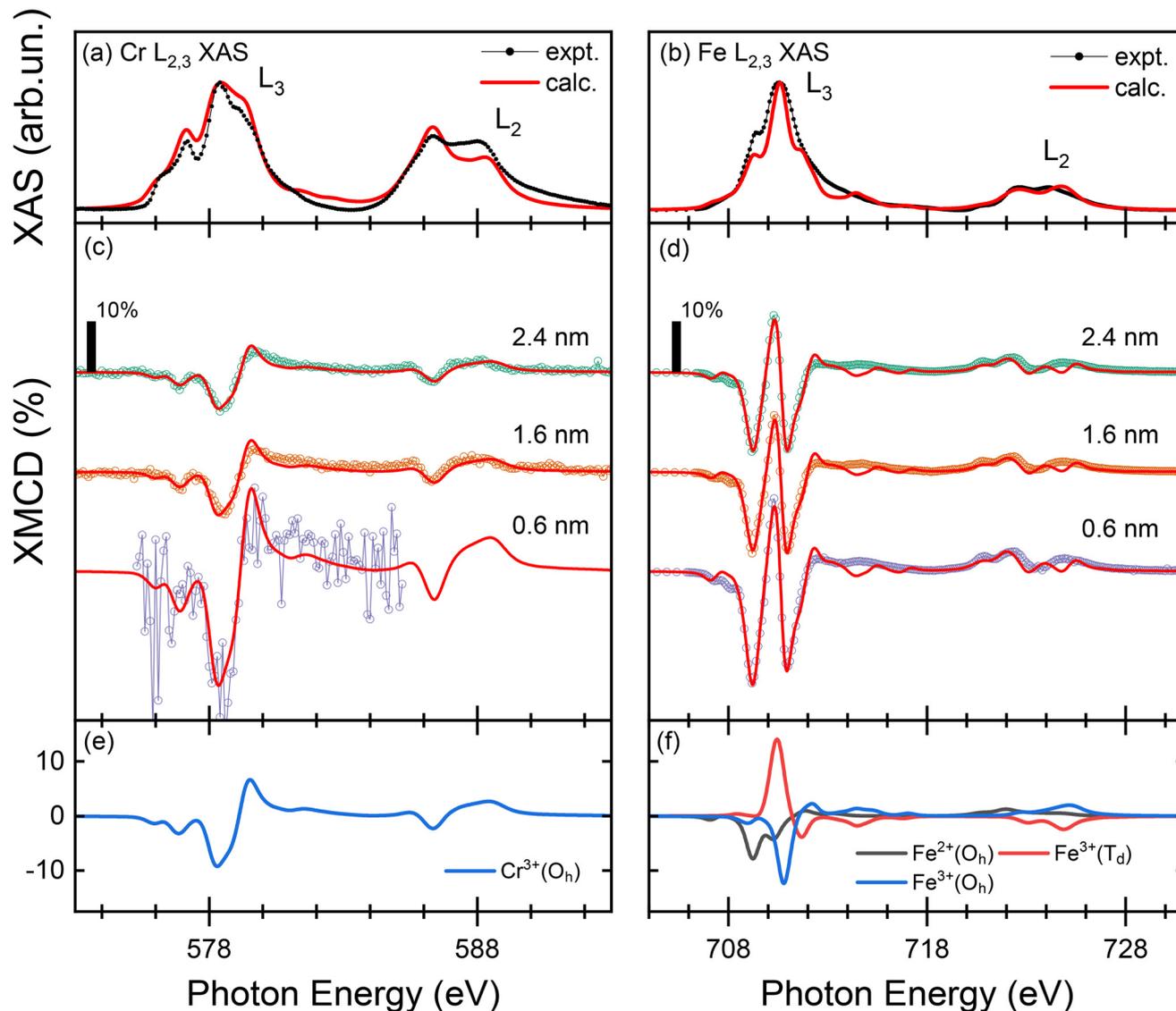
Fig. 4 XAS/XMCD measurements at the Fe and Cr $L_{2,3}$ absorption thresholds. (a and b) Experimental (black dotted lines) and calculated (red lines) X-ray absorption curves. All spectra were collected at room temperature with the samples in the remanent state. (c and d) XMCD curves for different thicknesses of the $MgCr_2O_4$ spacer. The XMCD curves are normalized to the maximum average intensity of the L_3 absorption threshold in the respective Fe and Cr spectra. The XMCD curves are well reproduced by calculations (red lines) reported in panels (e and f). Calculated XMCD curves used to reproduce the experimental results. Details of the calculations are reported in the text.

tite,[70] the occurrence of a sizeable XMCD for Cr in $MgCr_2O_4$ is unexpected, as $MgCr_2O_4$ is an antiferromagnetic semiconductor with a Néel temperature of about 13 K and is paramagnetic at room temperature. Accordingly, we indeed found that the XMCD signal at the Cr $L_{2,3}$ absorption edges was vanishing in a single $MgCr_2O_4$ film (not shown). The XMCD curves of Cr and Fe ions in panels (c) and (d), respectively, show consistent lineshape but varying intensity with increasing spacer thickness. In particular, the trilayers with $MgCr_2O_4$ spacers of 1.6 nm and 2.4 nm show nearly identical XMCD spectral features and comparable amplitudes, indicating that both configurations result in effective magnetic decoupling of the Fe_3O_4 layers. Note that the calculation shown in Fig. 4(e),

indicating a sizable XMCD for the Cr^{3+} ions, does not take into account the whole $MgCr_2O_4$ structure. The sign of the XMCD curves for Fe and Cr indicates that the Cr magnetic moments are oriented as those of the $Fe^{2+/3+}$ ions in the octahedral sites of magnetite, thus ruling out the presence of Cr ions in the tetrahedral sites. This condition resembles the ferromagnetic state of Cr for the iron chromite $CrFe_2O_4$,[65] where the Cr^{3+} ions only occupy lattice sites with O_h symmetry. Furthermore, the XMCD curves of Cr are fully consistent with the XMCD calculation shown in panel (e), based on the same configurational parameters of the absorption threshold, except for a scale factor adopted to fit the change of the experimental XMCD amplitude. This indicates the formation of mixed phases at

the $Fe_3O_4/MgCr_2O_4$ boundaries, in which the replacement of Fe by Cr in the lattice promotes the magnetic ordering of the Cr magnetic moments.

To investigate this replacement process in the Fe_3O_4 lattice, we analysed in detail the lineshape of the Fe XMCD curves in the L_3 energy region. In Fig. 5, the XMCD curves for the samples with the thinner (0.6 nm) and thicker (2.4 nm) $MgCr_2O_4$ spacer thicknesses, and for a 60 nm thick film of Fe_3O_4 used as a reference for the bulk, are normalized to the maximum XMCD. This procedure highlights the reduction of XMCD in the energy region associated with the Fe^{2+} contribution upon increasing the $MgCr_2O_4$ spacer thickness. We evaluated the relative concentration of the Fe^{2+} (O_h), Fe^{3+} (T_d), and Fe^{3+} (O_h) components in the Fe XMCD curves by fitting the L_3 energy region with the three dichroic contributions shown in Fig. 4(f). This approach provided fruitful information in other cases involving Fe_3O_4 or Fe_2O_3.[64] As shown in Fig. 5, the fitting results obtained by proper weighting of the three dichroic contributions confirm the evolution of the experimental curves, with the relative amount of Fe^{2+} (O_h) : Fe^{3+} (T_d) : Fe^{3+} (O_h) passing from 0.92 : 1 : 1 for the thinner $MgCr_2O_4$ spacer to 0.85 : 1 : 1 for the thicker one.

Such behavior is consistent with a scenario in which Fe_3O_4 and $MgCr_2O_4$ diffuse at their interface, forming a mixed region, as also evidenced by the EDX-STEM results, where Cr^{3+}

partially replaces Fe^{2+} (in octahedral coordination), which can then be oxidized to Fe^{3+}.[71] This leads to the formation of a mixed spinel oxide at the $Fe_3O_4/MgCr_2O_4$ interfaces, containing both iron and chromium ions. Compared to pure Fe_3O_4, this phase exhibits lower saturation magnetization and softer magnetic properties, which is in agreement with the literature data on mixed Cr/Fe spinel oxides.[59] In this phase, Cr^{3+} ions acquire magnetic polarization, and the relative proportions of iron species in Fe_3O_4 are modified, consistent with the characteristics of mixed Cr/Fe spinel oxides. As a result, the enhanced XMCD signal observed in the thinner $MgCr_2O_4$ layer [~20%, as shown in Fig. 4(c)] may be linked to the low chromium content at the interface. As the thickness of the $MgCr_2O_4$ layer increases, more Cr ions are available to diffuse through the interface, leading to the formation of a mixed Cr/Fe spinel phase with a higher chromium concentration, compatible with a decrease in the Cr XMCD signal and in a decrease in the coercive field, as observed by Pinho et al.[59]

It has to be noted that in a complex system such as magnetite, characterized by the interaction of different Fe valences, the exact balance between the various Fe ions is fundamental for establishing certain magnetic behaviours. For example, it is quite common that in Fe_3O_4 films, an Fe(octahedral)–O termination is the most favourable,[72] and, in general, it has been reported that the Fe_3O_4 surface is richer in Fe^{3+} (O_h) than the bulk,[73,74] leading to a decrease in the saturation magnetization. In particular, in the present case, the exact nature of the $Fe_3O_4/MgCr_2O_4$ interface could play a role in the magnetic behaviour of the investigated heterostructures. In this respect, it might be helpful to quantify the magnetic moment of iron in Fe_3O_4 via the XMCD sum rules,[75] keeping in mind that the obtained values may have some uncertainties due, for example, to the exact value of the number of 3d holes used (here 13.5 for all the samples) and the integration range for magnetic moment estimation.[62,76] As a consequence, the absolute values of the obtained magnetic moments might be questionable, while a relative comparison among the values obtained for the different samples remains reliable. The values of the spin (μ_{spin}), orbital (μ_{orb}) and total (μ) Fe magnetic moments in the three investigated trilayers, the 60 nm thick Fe_3O_4 grown on MgO(100) and the 7 nm thin Fe_3O_4 grown on $MgCr_2O_4/MgAl_2O_4$ (100), are collected in Table 2.

The iron magnetic moment of the trilayer with the thinnest $MgCr_2O_4$ spacer is basically equal to that of the 60 nm thick reference Fe_3O_4 sample (both values being, however, lower than the bulk value) and larger than that of a single 7 nm
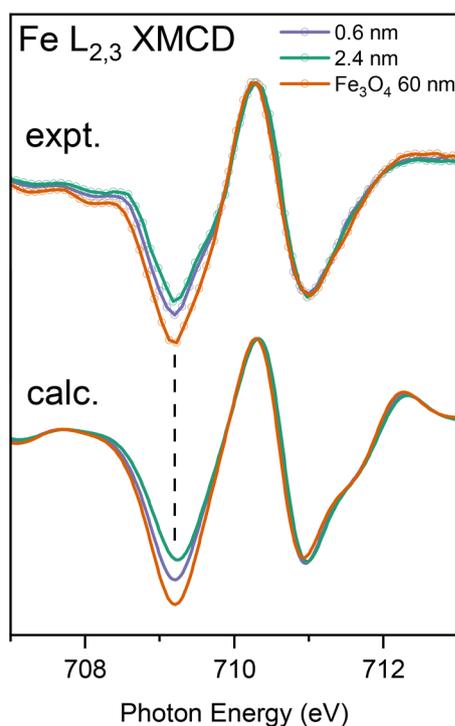

Fig. 5 Experimental and theoretical XMCD curves at the Fe L_3 absorption threshold for different $MgCr_2O_4$ thicknesses and the reference Fe_3O_4 thick layer. The XMCD curves are normalized to the maximum to emphasize the change in the low energy region. The theoretical XMCD curves were obtained by fitting the contribution of the different Fe ions in the Fe_3O_4 lattice.

Table 2 Fe magnetic moments obtained by XMCD sum rules

Sample	μ_{spin} (μ_B)	μ_{orb} (μ_B)	μ (μ_B)
60 nm Fe_3O_4	1.88	1.10	1.98
7 nm Fe_3O_4	1.11	0.30	1.41
0.6 nm $MgCr_2O_4$	1.84	0.17	2.01
1.6 nm $MgCr_2O_4$	1.51	0.07	1.58
2.4 nm $MgCr_2O_4$	1.36	0.15	1.51

Fe_3O_4 film (corresponding XMCD spectra not shown in Fig. 4 and reported in the ESI Fig. SI12†). This observation suggests that the thinnest $MgCr_2O_4$ spacer does not fully decouple the two magnetite layers, causing the heterostructure to behave as a single Fe_3O_4 ferromagnetic film with an equivalent thickness of approximately 15 nm, as if the layers are in direct contact. In contrast, for $MgCr_2O_4$ spacers of ≥ 1.6 nm, the magnetic moment in Fe_3O_4 decreases significantly to values similar to those of a single 7 nm Fe_3O_4 film. This indicates that the two layers behave almost independently, as they are effectively decoupled by the $MgCr_2O_4$ spacer, with the $Cr_xFe_{3-x}O_4$ phase being confined to the boundaries with Fe_3O_4, consistent with conclusions drawn from the magnetization curves. Indeed, the incorporation of Cr into Fe_3O_4, with the formation of the $Cr_xFe_{3-x}O_4$, results in a reduction of the Fe magnetic moment with respect to pure magnetite,[59] thus if this alloy phase had not been limited to the interface alone, an even greater reduction in magnetic moments would have been observed.

4. Conclusions

Epitaxial all-spinel $Fe_3O_4/MgCr_2O_4/Fe_3O_4$ heterostructures with variable spacer thicknesses were thoroughly investigated with a combination of chemical, morphological, structural, magnetic, and surface characterization studies. For spacer thicknesses of ≥ 1.6 nm, the two magnetite layers are effectively decoupled and behave as independent ferrimagnetic layers, thus demonstrating the feasibility of designing intricate all-oxide heterostructures that retain the intrinsic properties of individual thin Fe_3O_4 films. These samples exhibit relatively low coercivity, which is attributed to a reduced presence of antiphase boundaries due to the excellent lattice match between Fe_3O_4 and $MgCr_2O_4$ buffer layers. Limited cation interdiffusion occurs at the $Fe_3O_4/MgCr_2O_4$ interface, resulting in the formation of a mixed Cr/Fe spinel oxide phase localized at the interphase boundaries, which does not significantly affect the overall magnetic properties, remaining largely consistent with those of the individual Fe_3O_4 layers. This study provides insights into the magnetic interactions between Fe_3O_4 layers mediated by an $MgCr_2O_4$ spacer, demonstrating that thin Fe_3O_4 films can retain their intrinsic properties within complex heterostructures, paving the way for advanced all-spinel oxide devices with tailored functionalities.

Author contributions

Francesco Offi: conceptualization, data curation, formal analysis, investigation, methodology, writing – original draft, and writing – review & editing; Francesco Borgatti: data curation, formal analysis, investigation, methodology, writing – original draft, and writing – review & editing; Pasquale Orgiani: investigation, methodology, and writing – original draft; Vincent Polewczyk: data curation, formal analysis, investigation and writing – original draft; Sandeep Kumar Chaluvadi: data curation, investigation, and writing – original draft; Shyni Punathum Chalil: data curation, investigation, and writing – original draft; Alexander Petrov: data curation, formal analysis, investigation, methodology, and writing – original draft; Federico Motti: data curation, investigation, and writing – original draft; Gian Marco Pierantozzi: data curation, investigation, and writing – original draft; Giancarlo Panaccione: funding acquisition, investigation, and writing – original draft; Bogdan Rutkowski: data curation, formal analysis, funding acquisition, investigation, methodology, and writing – original draft; Paolo Mengucci: writing – original draft; Gianni Barucca: investigation, methodology, and writing – original draft; Deepnarayan Biswas: data curation, investigation, methodology, and writing – original draft; Tien-Lin Lee: data curation, investigation, methodology, and writing – original draft; Emiliano Marchetti: formal analysis, methodology, and writing – original draft; Alberto Martinelli: methodology and writing – original draft; Davide Peddis: conceptualization, funding acquisition, investigation, and writing – original draft; Gaspare Varvaro: conceptualization, funding acquisition, writing – original draft, and writing – review & editing.

Data availability

The data supporting this article have been included as part of the ESI.†

Conflicts of interest

There are no conflicts to declare.

Acknowledgements

References

1 G. Varvaro, A. Omelyanchik and D. Peddis, in *Ferroic Transition Metal Oxide Nano-heterostructures: From Fundamentals to Applications*, John Wiley & Sons, Ltd, 2022, ch. 12, pp. 405–437.

2 S. Das, A. Ghosh, M. R. McCarter, S.-L. Hsu, Y.-L. Tang, A. R. Damodaran, R. Ramesh and L. W. Martin, *APL Mater.*, 2018, **6**, 100901.

3 A. Bhattacharya and S. J. May, *Annu. Rev. Mater. Res.*, 2014, **44**, 65–90.

4 V. Tsurkan, H.-A. Krug von Nidda, J. Deisenhofer, P. Lunkenheimer and A. Loidl, *Phys. Rep.*, 2021, **926**, 1–86.

5 S. Emori and P. Li, *J. Appl. Phys.*, 2021, **129**, 020901.

6 X. Wang, Y. Liao, D. Zhang, T. Wen and Z. Zhong, *J. Mater. Sci. Technol.*, 2018, **34**, 1259–1272.

7 M. Schmitt, O. Kirilmaz, S. Chernov, S. Babenkov, D. Vasilyev, O. Fedchenko, K. Medjanik, Y. Matveyev, A. Gloskovskii, C. Schlueter, A. Winkelmann, L. Dudy, H.-J. Elmers, G. Schönhense, M. Sing and R. Claessen, *Phys. Rev. B*, 2021, **104**, 045129.

8 L. S. Ganapathe, M. A. Mohamed, R. M. Yunus and D. D. Berhanuddin, *Magnetochemistry*, 2020, **6**, 68.

9 M. S. Ansari, M. H. D. Othman, M. O. Ansari, S. Ansari and H. Abdullah, *Appl. Mater. Today*, 2021, **25**, 101181.

10 M. Nichterwitz, S. Honnali, M. Kutuzau, S. Guo, J. Zehner, K. Nielsch and K. Leistner, *APL Mater.*, 2021, **9**, 030903.

11 L. Sun, Q. Zhao, L. Che, N. Li, X. Leng, Y. Long and Y. Lu, *Adv. Funct. Mater.*, 2024, **34**, 2311398.

12 J. López-Sánchez, A. Del Campo, A. Quesada, A. Rivelles, M. Abuín, R. Sainz, E. Sebastiani-Tofano, J. Rubio-Zuazo, D. A. Ochoa, J. F. Fernández, J. E. García and F. Rubio-Marco, *ACS Appl. Mater. Interfaces*, 2024, **16**, 19866.

13 L. Hu, X. Sun, F. Zhou, J. Qi, A. Wang, C. Wang, M. Liu and M. Feng, *Ceram. Int.*, 2021, **47**, 2672–2677.

14 G. Lavorato, E. Winkler, B. Rivas-Murias and F. Rivadulla, *Phys. Rev. B*, 2016, **94**, 054405.

15 K. Omori, T. Kawai, N. Takahashi, T. Yanase, T. Shimada and T. Nagahama, *Appl. Phys. Lett.*, 2017, **110**, 212402.

16 P. van der Zaag, P. Bloemen, J. Gaines, R. Wolf, P. van der Heijden, R. van de Veerdonk and W. de Jonge, *J. Magn. Magn. Mater.*, 2000, **211**, 301–308.

17 O. Mauit, K. Fleischer, C. O. Coileáin, B. Bulfin, D. S. Fox, C. M. Smith, D. Mullarkey, G. Sugurbekova, H. Zhang and I. V. Shvets, *Phys. Rev. B*, 2017, **95**, 125128.

18 H.-C. Wu, C. O. Coileain, M. Abid, O. Mauit, A. Syrlybekov, A. Khalid, H. Xu, R. Gatensby, J. J. Wang, H. Liu, L. Yang, G. S. Duesberg, H.-Z. Zhang, M. Abid and I. V. Shvets, *Sci. Rep.*, 2015, **5**, 15984.

19 H.-C. Wu, S. K. Arora, O. N. Mryasov and I. V. Shvets, *Appl. Phys. Lett.*, 2008, **92**, 182502.

20 G. Chern, L. Horng, W. K. Shieh and T. C. Wu, *Phys. Rev. B*, 2001, **63**, 094421.

21 A. Orozco, S. B. Ogale, Y. H. Li, P. Fournier, E. Li, H. Asano, V. Smolyaninova, R. L. Greene, R. P. Sharma, R. Ramesh and T. Venkatesan, *Phys. Rev. Lett.*, 1999, **83**, 1680–1683.

22 P. A. A. van der Heijden, P. J. H. Bloemen, J. M. Metselaar, R. M. Wolf, J. M. Gaines, J. T. W. M. van Eemeren, P. J. van der Zaag and W. J. M. de Jonge, *Phys. Rev. B*, 1997, **55**, 11569–11575.

23 F. Motti, L. J. Riddiford, D. Vaclavkova, S. Sahoo, A. Milenko Müller, C. Vockenhuber, A. Baghi Zadeh, C. Piamonteze, C. W. Schneider, V. Scagnoli and L. J. Heyderman, *Phys. Rev. B*, 2023, **108**, 104426.

24 O. Toktarbaiuly, A. Syrlybekov, O. Mauit, A. Kurbanova, G. Sugurbekova and I. Shvets, *Mater. Today: Proc.*, 2022, **49**, 2469.

25 X. W. Li, A. Gupta, G. Xiao, W. Qian and V. P. Dravid, *Appl. Phys. Lett.*, 1998, **73**, 3282.

26 M. G. Brik, A. Suchocki and A. Kamińska, *Inorg. Chem.*, 2014, **53**, 5088–5099.

27 M. C. Kemei, P. T. Barton, S. L. Moffitt, M. W. Gaultois, J. A. Kurzman, R. Seshadri, M. R. Suchomel and Y.-I. Kim, *J. Phys.: Condens. Matter*, 2013, **25**, 326001.

28 F. Wen, X. Liu, M. Kareev, T.-C. Wu, M. Terilli, J. Chakhalian, P. Shafer and E. Arenholz, *Phys. Rev. B*, 2020, **102**, 165426.

29 B. Chen, H. Xu, C. Ma, S. Mattauch, D. Lan, F. Jin, Z. Guo, S. Wan, P. Chen, G. Gao, F. Chen, Y. Su and W. Wu, *Science*, 2017, **357**, 191–194.

30 P. Orgiani, S. K. Chaluvadi, S. P. Chalil, F. Mazzola, A. Jana, S. Dolabella, P. Rajak, M. Ferrara, D. Benedetti, A. Fondacaro, F. Salvador, R. Ciancio, J. Fujii, G. Panaccione, I. Vobornik and G. Rossi, *Rev. Sci. Instrum.*, 2023, **94**, 033903.

31 J. A. Moyer, R. Gao, P. Schiffer and L. W. Martin, *Sci. Rep.*, 2015, **5**, 10363.

32 A. Di Trolio, P. Alippi, E. M. Bauer, G. Ciatto, M. H. Chu, G. Varvaro, A. Polimeni, M. Capizzi, M. Valentini, F. Bobba, C. Di Giorgio and A. Amore Bonapasta, *ACS Appl. Mater. Interfaces*, 2016, **8**, 12925.

33 G. Varvaro, A. Di Trolio, A. Polimeni, A. Gabbani, F. Pineider, C. de Julián Fernández, G. Barucca, P. Mengucci, A. Amore Bonapasta and A. M. Testa, *J. Mater. Chem. C*, 2019, **7**, 78.

34 C. Yu, A. S. Sokolov, P. Kulik and V. G. Harris, *J. Alloys Compd.*, 2020, **814**, 152301.

35 S. K. Chaluvadi, S. P. Chalil, F. Mazzola, S. Dolabella, P. Rajak, M. Ferrara, R. Ciancio, J. Fujii, G. Panaccione, G. Rossi and P. Orgiani, *Sci. Rep.*, 2023, **13**, 3882.

36 M. Luysberg, R. G. S. Sofin, S. K. Arora and I. V. Shvets, *Phys. Rev. B*, 2009, **80**, 024111.

37 G. Vinai, F. Motti, A. Y. Petrov, V. Polewczyk, V. Bonanni, R. Edla, B. Gobaut, J. Fujii, F. Suran, D. Benedetti, F. Salvador, A. Fondacaro, G. Rossi, G. Panaccione, B. A. Davidson and P. Torelli, *Rev. Sci. Instrum.*, 2020, **91**, 085109.

38 G. Panaccione, I. Vobornik, J. Fujii, D. Krizmancic, E. Annese, L. Giovanelli, F. Maccherozzi, F. Salvador, A. De Luisa, D. Benedetti, A. Gruden, P. Bertoch, F. Polack, D. Cocco, G. Sostero, B. Diviacco, M. Hochstrasser, U. Maier, D. Pescia, C. H. Back, T. Greber, J. Osterwalder,

M. Galaktionov, M. Sancrotti and G. Rossi, *Rev. Sci. Instrum.*, 2009, **80**, 043105.

39 T.-L. Lee and D. A. Duncan, *Synchrotron Radiat. News*, 2018, **31**, 16.

40 *FEI application note AN002707*-2010, technical report, 2010.

41 M. W. Haverkort, M. Zwierzycki and O. K. Andersen, *Phys. Rev. B*, 2012, **85**, 165113.

42 F. de Groot and A. Kotani, *Core Level Spectroscopy of Solids*, CRC Press, 1st edn, 2008.

43 M. Rudee, D. Margulies and A. Berkowitz, *Microsc. Microanal.*, 1997, **3**, 126–129.

44 Y. Zhang, M.-G. Han, D. Sando, L. Wu, N. Valanoor and Y. Zhu, *ACS Appl. Electron. Mater.*, 2021, **3**, 3226–3233.

45 T. Fujii, F. M. F. de Groot, G. A. Sawatzky, F. C. Voogt, T. Hibma and K. Okada, *Phys. Rev. B*, 1999, **59**, 3195–3202.

46 J. Rubio-Zuazo, A. Chainani, M. Taguchi, D. Malterre, A. Serrano and G. R. Castro, *Phys. Rev. B*, 2018, **97**, 235148.

47 A. P. Grosvenor, B. A. Kobe, M. C. Biesinger and N. S. McIntyre, *Surf. Interface Anal.*, 2004, **36**, 1564–1574.

48 D. D. Hawn and B. M. DeKoven, *Surf. Interface Anal.*, 1987, **10**, 63.

49 A. Gota, E. Guiot, M. Henriot and M. Gautier-Soyer, *Phys. Rev. B*, 1999, **60**, 14387.

50 M. C. Biesinger, C. Brown, J. R. Mycroft, R. D. Davidson and N. S. McIntyre, *Surf. Interface Anal.*, 2004, **36**, 1550–1563.

51 P. Vasconcelos Borges Pinho, A. Chartier, J.-B. Moussy, D. Menut and F. Miserque, *Materialia*, 2020, **12**, 100753.

52 Z. Q. Qiu and S. D. Bader, *Rev. Sci. Instrum.*, 2000, **71**, 1243.

53 J.-B. Moussy, S. Gota, A. Bataille, M.-J. Guittet, M. Gautier-Soyer, F. Delille, B. Dieny, F. Ott, T. D. Doan, P. Warin, P. Bayle-Guillemaud, C. Gatel and E. Snoeck, *Phys. Rev. B*, 2004, **70**, 174448.

54 P. K. J. Wong, W. Zhang, X. G. Cui, Y. B. Xu, J. Wu, Z. K. Tao, X. Li, Z. L. Xie, R. Zhang and G. van der Laan, *Phys. Rev. B*, 2010, **81**, 035419.

55 A. Bollero, M. Ziese, R. Höhne, H. Semmelhack, U. Köhler, A. Setzer and P. Esquinazi, *J. Magn. Magn. Mater.*, 2005, **285**, 279–289.

56 A. V. Singh, B. Khodadadi, J. B. Mohammadi, S. Keshavarz, T. Mewes, D. S. Negi, R. Datta, Z. Galazka, R. Uecker and A. Gupta, *Adv. Mater.*, 2017, **29**, 1701222.

57 V. V. Balashev, K. Ermakov, D. A. Tsukanov, A. Y. Samardak, A. V. Ognev and A. S. Samardak, *J. Alloys Compd.*, 2023, **961**, 170967.

58 J.-B. Moussy, *J. Phys. D: Appl. Phys.*, 2013, **46**, 143001.

59 P. Vasconcelos Borges Pinho, A. Chartier, D. Menut, A. Barbier, M. O. Hunault, P. Ohresser, C. Marcelot, B. Warot-Fonrose, F. Miserque and J.-B. Moussy, *Appl. Surf. Sci.*, 2023, **615**, 156354.

60 M. Abbate, J. B. Goedkoop, F. M. F. de Groot, M. Grioni, J. C. Fuggle, S. Hofmann, H. Petersen and M. Sacchi, *Surf. Interface Anal.*, 1992, **18**, 65.

61 S. Gota, M. Gautier-Soyer and M. Sacchi, *Phys. Rev. B*, 2000, **62**, 4187.

62 E. Goering, S. Gold, M. Lafkioti and G. Schütz, *Europhys. Lett.*, 2006, **73**, 97.

63 P. Kuiper, B. G. Searle, L. C. Duda, R. M. Wolf and P. J. Van Der Zaag, *J. Electron Spectrosc. Relat. Phenom.*, 1997, **86**, 107–113.

64 R. A. Pattrick, G. Van Der Laan, C. M. B. Henderson, P. Kuiper, E. Dudzik and D. J. Vaughan, *Eur. J. Mineral.*, 2002, **14**, 1095–1102.

65 S. A. Chambers, T. C. Droubay, T. C. Kaspar, I. H. Nayyar, M. E. McBriarty, S. M. Heald, D. J. Keavney, M. E. Bowden and P. V. Sushko, *Adv. Funct. Mater.*, 2017, **27**, 1605040.

66 C. Theil, J. van Elp and F. Folkmann, *Phys. Rev. B*, 1999, **59**, 7931–7936.

67 E. Gaudry, P. Sainctavit, F. Juillot, F. Bondioli, P. Ohresser and I. Letard, *Phys. Chem. Miner.*, 2006, **32**, 710–720.

68 H. Elnaggar, R. Wang, M. Ghiasi, M. Yañez, M. U. Delgado-Jaime, M. H. Hamed, A. Juhin, S. S. Dhesi and F. de Groot, *Phys. Rev. Mater.*, 2020, **4**, 024415.

69 K. Kuepper, O. Kuschel, N. Pathé, T. Schemme, J. Schmalhorst, A. Thomas, E. Arenholz, M. Gorgoi, R. Ovsyannikov, S. Bartkowski, G. Reiss and J. Wollschläger, *Phys. Rev. B*, 2016, **94**, 024401.

70 G. F. M. Gomes, T. E. P. Bueno, D. E. Parreiras, G. J. P. Abreu, A. de Siervo, J. C. Cezar, H.-D. Pfannes and R. Paniago, *Phys. Rev. B*, 2014, **90**, 134422.

71 N. D. Telling, V. S. Coker, R. S. Cutting, G. van der Laan, C. I. Pearce, R. A. D. Pattrick, E. Arenholz and J. R. Lloyd, *Appl. Phys. Lett.*, 2009, **95**, 163701.

72 G. S. Parkinson, U. Diebold, J. Tang and L. Malkinski, *Advanced Magnetic Materials*, IntechOpen, Rijeka, 2012, ch. 3, pp. 61–88.

73 S. Kaya, H. Ogasawara and A. Nilsson, *Catal. Today*, 2015, **240**, 184.

74 T. Pohlmann, M. Hoppe, J. Thien, A. B. Dey, A. Alexander, K. Ruwisch, O. Gutowski, J. Röh, A. Gloskovskii, C. Schlueter, K. Küpper, J. Wollschläger and F. Bertram, *Phys. Rev. B*, 2022, **105**, 045412.

75 C. T. Chen, Y. U. Idzerda, H.-J. Lin, N. V. Smith, G. Meigs, E. Chaban, G. H. Ho, E. Pellegrin and F. Sette, *Phys. Rev. Lett.*, 1995, **75**, 152.

76 D. J. Huang, C. F. Chang, H.-T. Jeng, G. Y. Guo, H.-J. Lin, W. B. Wu, H. C. Ku, A. Fujimori, Y. Takahashi and C. T. Chen, *Phys. Rev. Lett.*, 2004, **93**, 077204.